Review Paper https://doi.org/10.7733/jnfcwt.2022.005

Corrosion of Containment Alloys in Molten Salt Reactors and the Prospect of Online Monitoring

Thomas Hartmann* and Patricia Paviet
Pacific Northwest National Laboratory, 902 Battelle Blvd, Richland, Washington 99354, USA

(Received July 27, 2021 / Revised September 14, 2021 / Approved September 23, 2021)

The aim of this review is to communicate some essential knowledge of the underlying mechanism of the corrosion of structural containment alloys during molten salt reactor operation in the context of prospective online monitoring in future MSR installations. The formation of metal halide species and the progression of their concentration in the molten salt do reflect containment corrosion, tracing the depletion of alloying metals at the alloy salt interface will assure safe conditions during reactor operation. Even though the progress of alloying metal halides concentrations in the molten salt do strongly understate actual corrosion rates, their prospective 1st order kinetics followed by near-linearly increase is attributed to homogeneous matrix corrosion. The service life of the structural containment alloy is derived from homogeneous matrix corrosion and near-surface void formation but less so from intergranular cracking (IGC) and pitting corrosion. Online monitoring of corrosion species is of particular interest for molten chloride systems since besides the expected formation of chromium chloride species $CrCl_2$ and $CrCl_3$, other metal chloride species such as $FeCl_2$, $FeCl_3$, $MoCl_2$, $MnCl_2$ and $NiCl_2$ will form, depending on the selected structural alloy. The metal chloride concentrations should follow, after an incubation period of about 10,000 hours, a linear projection with a positive slope and a steady increase of < 1 ppm per day. During the incubation period, metal concentration show 1st order kinetics and increasing linearly with time$^{1/2}$. Ideally, a linear increase reflects homogeneous matrix corrosion, while a sharp increase in the metal chloride concentration could set a warning flag for potential material failure within the projected service life, e.g. as result of intergranular cracking or pitting corrosion. Continuous monitoring of metal chloride concentrations can therefore provide direct information about the mechanism of the ongoing corrosion scenario and offer valuable information for a timely warning of prospective material failure.

Keywords: Containment corrosion, Molten salt reactors, Chromium, Chloride salt systems

*Corresponding Author.
Thomas Hartmann, Pacific Northwest National Laboratory, E-mail: thomas.hartmann@pnnl.gov, Tel: +1-208-346-0273

ORCID
Thomas Hartmann http://orcid.org/0000-0002-3192-5052 Patricia Paviet http://orcid.org/0000-0002-7759-2038

This is an Open-Access article distributed under the terms of the Creative Commons Attribution Non-Commercial License (http://creativecommons.org/licenses/by-nc/3.0) which permits unrestricted non-commercial use, distribution, and reproduction in any medium, provided the original work is properly cited

1. Introduction and Background

In the past decade, research & development efforts on advancing nuclear reactor technology have mostly focused on the design of Molten Salt Reactor (MSR) systems operating with thermal or fast neutron spectra for a potential deployment envisioned in the 2030s. At this, halide salt melts are considered as solvent for the fissile/fissionable content and/or as coolant. Fluoride salts have been considered since the early days of MSR technology in the 1960s, and chemical compatibility data of fluoride salt melts with Hastelloy N (standard and modified) are available since the inception of Molten Salt Reactor Experiment (MSRE) and the Accelerator-driven Transmutation Technology (ADTT) [1-6]. Related research on high-temperature molten-salts as liquid fuel and/or as primary coolant focused on fluoride salts because of their relatively noncorrosive behavior, neutron moderation, and the chemical stability at temperatures of 700°C. Chloride salts on the other hand, are an alternative option and considered by the latest commercial designs e.g. of Elysium MCSFR, TerraPower MCFR, Moltex SSR-W300 [7-9], but their performance is less well understood and additional data are needed for technological deployment and licensing. Chloride salt melts are lesser moderators and allow for a faster (harder) neutron spectrum. The deployment of a harder neutron spectrum allows spent nuclear fuel as potential fissile fuel source and therefore low long-term operational costs. Chloride melts are sufficient solvents for actinides and lanthanides, but as a result of the low electrochemical potentials of metal chlorides compared with metal fluorides, chloride salt systems in general show enhanced corrosion rates compared with fluoride salt systems. Chloride-based salts have been used in the fuel-reprocessing scheme developed for the integral fast reactor [10]. Experiments on corrosion effects with molten salts date back to the Aircraft Reactor Experiment as early as 1940 [1] and research on chemical compatibility of steel alloys with fluoride and chloride salts will continue in the coming years. Corrosion processes for chlorine are more complex than those for fluorine. Consequently, the knowledge base for structural materials tolerant to chloride-based salts is not as mature as the one for fluoride-based salts [10]. A confident structural material selection cannot yet be provided for any chloride salt-based molten salt reactors. The research discussed here does not directly aim to address this troubling problem but will, on the other hand, target the development of a useful tool to online monitor corrosion progress under molten salt reactor conditions, independent of materials selection. Corrosion of stainless steel (typically > 11wt% Cr) is initiated by the solubility of Cr as $CrCl_2$ or as $CrCl_3$ species in molten chloride salts, independent if Ni-based stainless steel (Hastelloy N also known as Alloy N), austenitic stainless steel (e.g. SS-316L) or ferritic-martensitic stainless steels (e.g. HT-9, T91) are deployed. Independent of the selected containment structural material, Cr does not form protective Cr_3O_4 chromite layers nor protective $FeCr_2O_4$ magnetite or spinel-type layers in molten chloride salts, but because of their low electrochemical potentials, chromium dissolves as $CrCl_2$ and $CrCl_3$ chloride species.

The dissolution of chromium and the subsequent formation of chromium chloride species under ideal conditions (homogeneous corrosion) can be described by a first order reaction kinetic (incubation period) followed by a linear concentration increase over time. During reactor operation, chromium chloride species form permanently at the alloy-salt interface with progressing concentration within the molten salt of sub-ppm level per day, in average. Under ideal conditions, this constant and steady increase of the chromium chloride species concentrations confirms a (safe) homogeneous matrix corrosion mechanism. Alterations of this linear increase with time could, on the other hand, signal additional overlaying mechanisms derived e.g. from pitting corrosion, intergranular cracking, the effects from salt impurities, and from the buildup of fission product (tellurium and lanthanides). Online monitoring of fluorinated or chlorinated alloy constituency can therefore aid reactor operation by providing information on the yield and

the characteristic of containment corrosion. However, additional (test-loop) experiments are needed to allow for an enhanced understanding and to break down the complexity of the overall corrosion mechanism and the subsequent formation of chromium halides under the conditions of MSR operation.

2. Chloride Salt Systems

MSR fuel salts serve multiple functions such as fuel, moderator, negative thermal feedback mechanism, heat transfer medium, and natural circulation mechanism for decay heat removal [10]. Chlorine shows several oxidation numbers (+7, +5, +3, −1) and therefore bonding configurations, solution and corrosion chemistry of chloride molten salts are more complex than those of fluorides. Also, actinide trichlorides show high solubilities and form lower melting point solutions with chloride salts. The simple binary NaCl-UCl_3 and NaCl-$PuCl_3$ systems e.g. show low eutectic melting at 520°C and 453°C with highest solubilities of UCl_3 and $PuCl_3$ of 32mol% and 36mol%, respectively [10]. NaCl provide good nuclear, chemical, and physical properties but an additional diluent salt might be required to adjust for mixture melting temperature and sufficiently low viscosities in the temperature range between 500°C and 700°C. Possible candidates for the additional diluent chloride salt are KCl, LiCl, but also $MgCl_2$.

The use of heavier cation chlorides promotes a harder (faster) neutron spectrum which will also require increasing the density of the fissile salt constituency mainly ^{235}U, ^{239}Pu, or ^{233}U if a thorium cycle is considered. Consequently, the total actinide chloride content including fissile and fertile isotopes is significant and will target 50% in weight. Burnup calculations e.g. for TerraPower MCFR were conducted with a simplified starting inventory of about 52mol% ^{238}U, 6.5mol% ^{239}Pu, 5.6mol% ^{23}Na, and 36.2mol% ^{37}Cl [12].

A simplified chloride fast reactor fuel system is represented by the binary eutectic systems NaCl-UCl_3 and NaCl-UCl_4. The binary system NaCl-UCl_3 alone cannot act as a surrogate system to accurately describe molten chloride fast reactor fuel systems because of its insufficient actinide solubilities. The system NaCl-UCl_3 shows no actinide solubility below 525°C and UCl_3 solubilities between 25mol% and 43mol% at 600°C. The binary NaCl-UCl_4 system, on the other hand, could be regarded as simplified model fuel system because of its wide actinide solubility range above 500°C which is caused by the presence of the congruent melting chloride phase Na_2UCl_6, sandwiched between two eutectics, at 30mol% UCl_4 and 47mol% UCl_4, respectively. As a result, at 500°C NaCl can dissolve between 28mol% and 75mol% UCl_4. This rather sufficient solubility range increases further towards higher temperatures (Fig. 1).

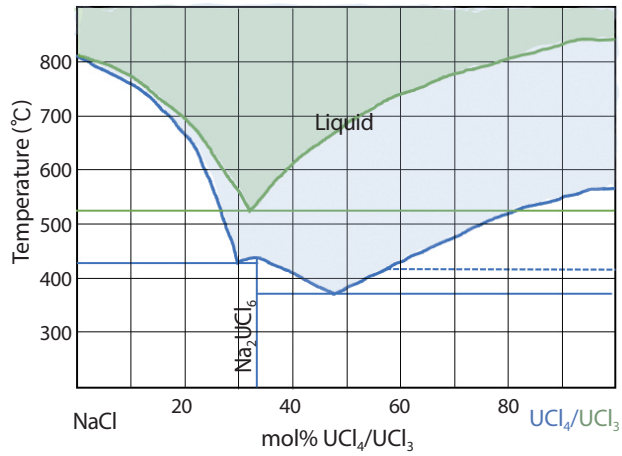

Fig. 1. Uranium solubility and liquid phase field in the NaCl-UCl_3 system (green sketch) vs. in the NaCl-UCl_4 system (blue sketch). Solubility data from R.E. Thoma [12] have been adapted.

In the past, in molten salt reactor applications using fluoride salt systems at Oak Ridge (e.g. Molten Salt Reactor Experiment) [13] or in Russia (MOSART) [5] an actinide species ratio UF_4/UF_3 of 500 was measured, representing equilibrium conditions. For chloride based MSR designs actual UCl_4/UCl_3 chloride species ratios have not been reported, while proprietary data may exist. If a U(VI)/U(III) species ratio of ~50 to ~500 is realistic for the chloride system as well, the two binary systems NaCl-UCl_3 and NaCl-UCl_4 could indeed be regarded as acceptable simplified

binary model systems for thermal and fast chloride based MSR fuel systems.

3. Stainless-Steel Containment and Structural Materials

The corrosion processes for chlorides are more complex than those for fluorides and the knowledge base for structural materials compatibility with chloride-based salt melts is far less mature than it is for fluoride-based salt systems [10]. As a consequence, a confident structural material selection cannot yet be provided for any chloride salt-based molten salt reactor systems. In the following, a selection of promising alloys and stainless-steel candidates will be introduced. These candidates can be grouped in three major categories: the families of Ni-based alloys; ferritic-martensitic stainless steels; and austenitic stainless steels.

3.1 Nickel-based Mo-Cr Hastelloy N Family

Since the very early days of the technological development of fluid fuel nuclear reactors, nickel-based alloys have been regarded as the containment material of choice because of their superior compatibility in corrosive media [14]. Early candidates such as Inconel, INOR-8 (later named Alloy N or Hastelloy N) or Hastelloy B (were Cr is replaced by Mo) were selected and tested using convection loop-type corrosion tests. Loop-type corrosion testing is still considered as state-of-the-art and provides the most accurate data mostly free of artefacts. Later during the Molten Salt Reactor Experiment (MSRE) Ni-based Mo-Cr Hastelloy N (balance Ni, 15–17% Mo, 6–8% Cr, 4–6% Fe, 0.04–0.08% C) was specifically designed and optimized for low homogeneous corrosion rates in fluoride salt melts, low susceptibility for grain boundary embrittlement by fission tellurium (modified Hastelloy N by the addition of 1–2wt% Nb and/or Ti), high-temperature tolerance, and fairly low radiation-induced void swelling [5, 6]. Because of its high nickel content, Hastelloy N is a far more expensive material than stainless steel and not as available, but most importantly, it suffers from softening and decreased tensile properties at temperatures above 700°C. Additionally, based on their face-centered cubic (fcc) crystal structure, Ni-based alloys show void swelling and tend to embrittle when exposed to core levels of neutron flux in excess of 10^{20} neutron cm^{-2} even at temperatures as high as of 500°C to 650°C. Even though Hastelloy-N shows superior chemical compatibility with halide salt melts, it is not yet approved by the Nuclear Regulatory Commission (NRC) as nuclear structural material because of radiation embrittlement, irradiation void swelling, and its low strength at temperatures above 700°C, which has to be considered in potential accident scenarios. However, niobium-modified Hastelloy N has the best chances of any Ni-based alloys for NRC certification, but more supporting information on radiation embrittlement and irradiation induced void swelling must become available. Hastelloy N is therefore still considered for potential use as reactor vessel, core barrel, control rod system, piping and pumps in primary and secondary coolant loops, and as primary and secondary heat exchangers.

3.2 Ferritic-Martensitic Stainless Steel

Ferritic-martensitic (FM) stainless-steels such as HT-9, EUROFER, or T91 show chemical and mechanical properties which can be regarded as rather reverse of those of the Ni-based Hastelloy N family. Ferritic-martensitic steels are 400-level steels and not considered chemically compatible with fluoride- and chloride salt melts at temperatures relevant for MSR deployment. On the other hand, they are simple to manufacture and rather inexpensive to fabricate since the content in alloying metals (Mn, Cr, Ni) is low. Most importantly, ferritic-martensitic steel show exceptionally good neutron flux tolerance, also thanks to their less-dense bcc (body-centered cubic) crystal structure. But it must be pointed out, that qualifying data on the chemical compatibility of high-Cr ferritic-martensitic steel

alloys with chloride salt melts are unavailable or lacking. No quantitative corrosion data of e.g. HT-9 in chloride salt melts have been published and little is known about the behavior of ferritic-martensitic steels under conditions related to chloride-based MSR operation, even if internal research reports e.g. by TerraPower, Elysium, or Moltex might exist. The consideration of FM stainless steels for molten chloride salt application utilizing a fast neutron spectrum are purely derived from the fact of their superior performance under neutron irradiation with neutron flux well above 10^{22} n·cm^{-2} at MSR relevant temperatures. FM steel such as HT-9 was developed by Sandvik, Sweden, for energy application and deployed as structural material at EBR-II at the INL and for fuel ducts at the FFTF (Fast Flux Test Facility) at the Hanford Site. The vast amount of qualifying radiation data on HT-9 showed significantly lower irradiation swelling for FM steel compared with austenitic stainless steels such as SS-316 at radiation damage levels of up to 155 dpa (displacements per atom). The tendency for helium embrittlement is far less for FM steel than for Ni-based alloys or austenitic stainless steel, besides of phase equilibration and transformation and the formation of silicide and carbide inclusions. However, FM steels are 400 level steels and not compatible with corrosive environments, also mechanical strength of FM steels decreases greatly at higher temperatures due to microstructural equilibration, coarsening, and the partly decomposition of the martensite phase. Materials selection for fast chloride MSR systems is most challenging and heavily nickel-clad ferritic-martensitic steel could probably serve as vessel and piping material [10].

3.3 Austenitic Stainless Steels SS-304 and SS-316

Austenitic stainless steels such as SS-304H and SS-316H possess fcc crystal structures and are viable candidates and NRC-approved structural materials for MSR designs. While SS-304H is considered as baseline structural material, SS-316H is used for reactor vessels, piping, and heat exchangers in primary and secondary loops [15]. SS-304 has excellent corrosion resistance in a wide range of media but is, in warm chloride media, subject to pitting and crevice corrosion. SS-304H has higher carbon content than SS-304L, which increases strength at temperatures above 500°C [16]. SS-304 serves as baseline material in some FHR (Fast High-temperature Reactors) designs and is available as nuclear grade SS-304 because of the experience obtained with light water reactors in the past. However, SS-304 is subject to Cr depletion in fluoride salts and its use in MSRs will be limited to components with no or limited contact to molten salts [15].

SS-316 has very similar mechanical and physical characteristics as SS-304 but because of higher nickel content, with much improved corrosion resistance, particularly to pitting corrosion in chloride environments [17]. SS-316 has excellent corrosion resistance in a wide range of media and an increased ability to resist pitting and crevice corrosion in warm chloride environments, but a continuous use in a 425–860°C temperature range is not recommended. SS-316 has demonstrated chemical compatibility in pure FLiBe and in the absence of neutron irradiation [18]. SS-316 may be an attractive structural material for FHR reactor vessel and there is significant experience with SS-316 in LWRs as fuel support. SS-316H is allowed for use at temperatures up to 816°C, is NRC codified, and more readily available than Hastelloy-N. SS-316 shows good tolerances to neutron irradiation compared with high-Ni superalloys like Hastelloy or Incoloy 800H, but far less so than ferritic-martensitic HT-9.

4. Thermodynamics of Corrosion Mechanism of Stainless Steel in Halide Salt Melts

Most engineering materials rely on the formation of a passive oxide film for corrosion protection. In molten halide salts, however, these protective films do not form. Corrosion of metal alloys depends largely on interfacial

Table 1. Potential corrosion indicator relative to the formation of $CrCl_2/CrCl_3$ for different containment alloys without considering self-diffusion coefficients and temperature, purely based on stoichiometry

Alloy	Metal	wt% in Alloy	Chloride Species	Potential corrosion indicator relative to chromium (Cr = 10) in disregard of kinetics
Hastelloy N	Mn	< 0.25	$MnCl_2$	0.3
	Cr	6–8	$CrCl_2$ / $CrCl_3$	10
	Ni	> 74.5	$NiCl_2$	93
	Mo	11–13	$MoCr_3$	16
	Fe	0.1	$FeCl_2$ / $FeCl_3$	0.13
	Ti	< 2	$TiCl_4$	< 2.5
HT-9	Mn	0.45	$MnCl_2$	0.5
	Cr	9	$CrCl_2$ / $CrCl_3$	10
	Ni	0.2	$NiCl_2$	0.2
	Mo	1	$MoCl_3$	1
	Fe	88.6	$FeCl_2$ / $FeCl_3$	98
SS-304	Mn	2	$MnCl_2$	1
	Cr	18–20	$CrCl_2$ / $CrCl_3$	10
	Ni	8–12	$NiCl_2$	6
	Fe	> 64.8	$FeCl_2$ / $FeCl_3$	32
SS-316	Mn	2	$MnCl_2$	1
	Cr	16–18	$CrCl_2$ / $CrCl_3$	10
	Ni	10–14	$NiCl_2$	7.8
	Mo	2–3	$MoCl_3$	1.5
	Fe	> 62	$FeCl_2$ / $FeCl_3$	34

reactions between molten salt and the bare metal surface and the underlaying thermodynamics can be derived through the free Gibbs energy of formation and the electrochemical potentials of the species involved. Alloy constituents tend to dissolve in reverse order of their nobility, and the most active element is most likely to dissolve. Therefore, the dissolution of elements in molten fluorides correlates well with the stability (energy of formation) of the metal fluoride species [4], and alloy constituents with the most negative (most stable) halides tend to be the most likely to dissolve. This thermodynamic driving force can explain the tendency for dissolution but does not account for total corrosion rates and the prospected service life of containment alloys. Kinetic information and subsequently quantitative data on homogeneous corrosion rates (e.g. 25−50 $\mu m \cdot year^{-1}$) can be eventually derived by the individual self-diffusion coefficients of each metal within an alloy at the given temperature, considering volume diffusivity and grain boundary diffusivity. Free Gibbs energy of formation for some fluoride and chloride are published by [19-21].

For all prospective MSR structural alloys introduced earlier, it can be stated that Cr is the most active major constituent since it is thermodynamically more favourable for Cr to form stable chlorides such as $CrCl_2$ and $CrCl_3$ rather than to remain an alloying constituent within the Ni-based alloy or the stainless steel matrix. Stainless steel in

general contains 11wt% Cr or more, and in chloride salt melts, chromium is the alloying constituent of highest chemical activity and oxidative corrosion at the steel-salt interface will show selective attack on chromium but also on Si, Al, Fe and Ni. Mo on the other hand, a major constituent of Hastelloy N, is rather stable in fluoride salt melts but less so in chloride salt melt and tends to form $MoCl_3$.

Computational data on redox potentials of salt and alloy species in fluoride and chloride salt melts have been published [21] and the stability of metal fluoride and metal chloride species in salt-fuel mixtures have been projected for actinide halide concentration ratios UF_4/UF_3 and UCl_4/UCl_3 of typically 500. Metal nobility based on thermodynamic calculation does also explain why chloride salt melts are more corrosive than fluoride salt melts. Under MSR conditions Cr, Mn, and (some) Fe will form fluoride as well as chloride species, while (most) Fe, Co, Ni, and Mo will go in solution dominantly as chloride species. As a result, the build-up and the progress in the concentration of a variety of metal chloride species in the molten salt depend on temperature, time and the deployed containment alloy. Corrosion of containment alloys and steels in chloride salt melts is ideally described by a 1st order kinetics followed by a linear increase in metal chloride concentration over time. Monitoring these metal chloride concentrations during MSR operation will provide valuable information on the magnitude and characteristics of containment corrosion. As a very simplified estimation and in disregard of any kinetic considerations, the potential concentrations of prospective metal chloride species for the composition of each alloy type are normalized relative to the formation of $CrCl_2/CrCl_3$ (Table 1). At this, the concentration of $CrCl_2/CrCl_3$ is arbitrarily set to a value of 10 for a relative comparison with other metal chlorides. In disregard of diffusion coefficients for each metal in the alloys, the rates for homogeneous corrosion of Hastelloy N could be traced through the formation of $NiCl_2$ and $MoCl_3$ together with $CrCl_2/CrCl_3$. Corrosion of ferritic-martensitic HT-9 and corrosion of austenitic SS-304 and SS-316 could also be monitored by the build-up of $FeCl_2/FeCl_3$ besides the formation of $CrCl_2/CrCl_3$ and their increasing concentration during ongoing corrosion.

For high-temperature application, the corrosion of the metallic containment alloy is the primary concern. Unlike the more conventional oxidizing media, the products of oxidation of metals by halide melts tend to be soluble in the oxidizing media [4]. The general rule to ensure that the structure materials are compatible with the salt melt is that the difference in the Gibbs free energy of formation between alloy and salt should be > 80 $kJ \cdot mol^{-1}$ [5]. Corrosion of structural MSR alloys in fluoride salt systems is well studied thanks to the early research on fluid fuelled reactors [1-6, 10]. This broad array on results and conclusions might serve as a blueprint when it comes to study the alloy compatibility in chloride systems. Corrosion in chloride salt systems is more complex and equilibrium concentrations of alloying constituents will strongly depend on the solvent systems. Therefore, this comparison has its limitations. In either system, free energies of formation for the alloy components (Mo, Cr, Fe, Ni) show that Cr is the most active alloying constituent. In this respect, stainless steel having more Cr than Ni-based alloys might be more susceptible to corrosion. Besides the long-term tendencies of corrosion dictated by thermodynamics and diffusion kinetics, impurities such as moisture, oxygen and other impurities can have noticeable short- and midterm impact in sealed systems. When the physical integrity of a corrosion loop is temporarily breached, corrosion is subsequently enhanced for a limited time.

Considering the corrosion-related relationships established for fluoride systems [5, 22] it might be safe to adapt these relationships for the chloride system as well. The following hypothetical reactions can be defined for either: 1) the presence of moisture, 2) the presence of oxide films, 3) the presence of impurities, and 4) the dissolution of alloy constituents due to the presence of UCl_4 which acts as oxidizer:

1) Presence of chloride with moisture can form insoluble metal oxides of higher melting points:

$$UCl_4 + 2H_2O \leftrightarrow UO_2 + 4HCl \quad (1)$$

Fuel oxide formation is traditionally prevented by the addition of ZrF_4, and eventually $ZrCl_4$ for chloride systems:

$$ZrCl_4 + 2H_2O \leftrightarrow ZrO_2 + 4HCl \quad (2)$$

This would result into an assumed net reaction of:

$$ZrCl_4 + UO_2 \leftrightarrow ZrO_2 + UCl_4 \quad (3)$$

2) Metal oxide films could be dissolved by chlorination as following:

$$2NiO + ZrCl_4 \leftrightarrow 2NiCl_2 + ZrO_2 \quad (4)$$

$$2NiO + UCl_4 \leftrightarrow 2NiCl_2 + UO_2 \quad (5)$$

$$2FeO + UCl_4 \leftrightarrow 2FeCl_2 + UO_2 \quad (6)$$

$$2Fe_2O_3 + 3CrCl_4 \leftrightarrow 3CrO_2 + 4FeCl_3 \quad (7)$$

3) Possible corrosion reaction with solvent components lacking purification:

$$Cr + NiCl_2 \leftrightarrow CrCl_2 + Ni \quad (8)$$

$$Cr + 2HCl \leftrightarrow CrCl_2 + H_2 \quad (9)$$

$$Cr + FeCl_2 \leftrightarrow CrCl_2 + Fe \quad (10)$$

4) Possible oxidative reaction of UCl_4 fuel phase with alloying constituents (Mo, Cr, Fe, Ni):

$$2UCl_4 + Mo \leftrightarrow 2UCl_3 + MoCl_2 \quad (11)$$

$$2UCl_4 + Cr \leftrightarrow 2UCl_3 + CrCl_2 \quad (12)$$

$$2UCl_4 + Fe \leftrightarrow 2UCl_3 + FeCl_2 \quad (13)$$

$$2UCl_4 + Ni \leftrightarrow 2UCl_3 + NiCl_2 \quad (14)$$

5. Kinetics and Mechanism of Structural Steel Corrosion in Halide Salt Melts

Alloying constituents tend to leach from the structural alloy into the molten halides based on the thermodynamic stability of their metal fluorides or metal chlorides. For most structural alloys, chromium is the major constituent to form stable halides. The selective depletion of Cr is widely accepted as the dominant form of materials degradation in molten halides. While the thermodynamic basis of chromium depletion is rather simple and straightforward, our knowledge about the underlying kinetics is not as settled. However, it is agreed that the yield of chromium self-diffusion in structural alloys does propel the kinetics of stainless-steel corrosion in molten halides. Therefore, an evaluation of diffusivity seems in order with the aim to define the fundamental mechanism and the yield of volume diffusivity and the more material-specific grain-boundary diffusivity.

5.1 Chromium Self Diffusivity in Ferritic/martensitic and Austenitic Stainless Steels

Redox processes responsible for the corrosion of structural alloys by molten fluoride mixtures result in selective oxidation of the contained chromium and other alloying metals. This dissolution of chromium from the alloy happens in regions of highest temperature and results in void formation near the alloys surface. Without the adverse impact of fission products such as tellurium, these voids are not restricted to grain boundaries, but are relatively uniformly distributed throughout the alloy surface and in close vicinity to the contact zone with the melt [3]. This corrosion scenario can be, as a first approximation, defined as homogeneous matrix corrosion and as the best-case scenario for containment corrosion in MSRs. The overall rate of corrosion was found to be controlled by the rate at which

chromium diffuses from the bulk to the surface where chromium will be dissolved by the salt melt [23] forming stable halides. Early measurements of the diffusion coefficient of Cr in Ni-based alloys (INOR-8, later named Alloy N) by profiling techniques using ^{51}Cr isotope determined the diffusion coefficients for Cr self-diffusion as 10^{-20} $m^2 \cdot s^{-1}$ to 10^{-16} $m^2 \cdot s^{-1}$ at 600°C and 900°C, respectively [23]. Self-diffusion coefficients and therefore containment corrosion are highly temperature sensitive. The temperature dependency of the diffusion coefficient D can be expressed by the Arrhenius-type equation:

$$D = D_0 \, e^{\frac{-Q}{RT}}; \text{ and } logD = \frac{-Q}{2.3RT} + logD_0 \qquad (15)$$

where D_0 represents a temperature-dependent pre-exponential or frequency factor and Q (or E) the activation energy ($J \cdot mol^{-1}$ or eV/atom). R is the gas constant (8.3144 $J \cdot K^{-1}$) and T the absolute temperature in K. The values for D_0 and Q are typically determined using the Arrhenius type relationship and were found to vary dependently on sample history such as manufacturing and heat treatment. For the MSR relevant temperature range, a strong contribution of grain-boundary diffusion was determined. Grain-boundary diffusion is, between 600°C and 750°C, decisive for the overall Cr mobility and the homogeneous corrosion rates of MSR containment alloys. At high temperatures of 800°C and above, the diffusion mechanism is basically described as volume or bulk diffusion and the contribution of grain-boundary diffusion at these high temperatures is minor. We can conclude that for structural alloys under MSR operation, diffusion along selective paths (grain boundaries) is dominant. In order to eventually quantify diffusion-based corrosion rates of chromium in structural alloys one must distinguish between the volume (bulk- or lattice-) self-diffusion coefficient (D_v) and a channel and grain boundary-based self-diffusion coefficient (D_b). To experimentally determine chromium diffusion coefficients, nickel-based alloys (Inconel, INOR-8) were fabricated and diffusion couples with alloys containing radioactive tracer (^{51}Cr, γ-emitter, 320 keV, λ = 27.7 days) were annealed in sealed fused silica ampules at different temperatures. The temperature-dependent ^{51}Cr self-diffusion coefficients in nickel-based alloys (Inconel, INOR-8) are extracted based on the ^{51}Cr diffusion paths [23].

Radiotracer ^{51}Cr diffusion experiments have further been conducted in 9–20wt% chromium ferritic and austenitic stainless steels [24]. At this, volume diffusion coefficients have been determined in the temperature range of 608°C to 1,008°C and values of grain-boundary diffusion coefficients between 522°C and 1,008°C were measured. The authors were considering type *B* diffusion [25], which is thought as the most obvious but also the most complicated case. The overall diffusion distance from (or towards) the surface of the solid is of the same order of magnitude as the scale of the dislocation network, and the concentration distribution does not approximate to any simple form. Therefore, a strict Fick's law behavior will not be observed at type *B* diffusion but it can be treated as described in the following.

The solution of Fick's law for volume diffusion is defined as:

$$C(X, t) = (M/\sqrt{\pi D_v t}) \, exp\left(\frac{-X^2}{4D_v t}\right) \qquad (16)$$

Where $C(X, t)$ is the concentration of the radioactive tracer (^{51}Cr) at distance X from the original surface, D_v the volume or lattice diffusion coefficient (in $m^2 \cdot s^{-1}$), t the time of the anneal and M the total amount of radioactive tracer for X, t = 0. This relationship represents materials transport within the crystal lattice through volume diffusion. The penetration profiles show a linear relationship between *ln C* (or *ln* γ-activity) vs. the square of the penetration distance X^2 as shown by Mizouchi et al. (2004) [26]. The direct volume diffusion contribution is defined as $(D_v t)^{1/2}$ (unit = m), where D_v is the volume diffusion coefficient and t the annealing time. If the volume diffusion contribution is smaller than the grain size (e.g. 10–15 μm) leakage of the diffusant (Cr) from the grain boundaries (GBs) towards the

bulk is permitted with none-negligible contribution. This regime shows diffusion profiles of complex shapes. At small reduced depths $\eta = x/(D_v t)^{1/2}$ where x is the depth from the diffusion source, the profiles are proportional to x^2 reflecting volume diffusion while for GB diffusion the logarithm of the mean concentration of the diffusant is proportional to $x^{6/5}$. To simultaneously determine volume diffusion coefficients as well as gain boundary diffusion, an analytical procedure to separate either contribution is needed. Considering a type *B* kinetics [25], the value of the mean diffusion distance $(D_v t)^{1/2}$ must be smaller than *1/20* for the average grain diameter d in the alloy microstructure, therefore: $d > 20\ (D_v t)^{1/2}$. For the diffusion of an instantaneous source the grain boundary diffusivity P is given by the triple product value as [27]:

$$P = D_b \delta k \tag{17}$$

and:

$$D_b \delta k = 1.308\ (D_v t)^{1/2} - \left(\frac{\partial ln C}{\partial X^{\frac{6}{5}}}\right)^{-\frac{5}{3}} = P\ (\text{unit: m}^3\cdot\text{s}^{-1}) \tag{18}$$

For an experimental D_b–D_v branching value β:

$$\beta = \frac{D_b \delta k}{D_v - 1} / 2(D_v t)^{\frac{1}{2}} > 10^4\ (\text{dimensionless}) \tag{19}$$

where D_b is the GB diffusion coefficient, δ the GB thickness, and k is a solute segregation factor [28], simply defined as ratio of diffusant concentration in GB over the diffusant concentration in the bulk. Considering self-diffusion, k is often equal to 1 and the GB thickness about 5 Å or 5×10^{-10} m. For *B* type diffusion the experimental D_b–D_v branching value β can also be defined as:

$$\beta = \frac{D_b - D_v}{D_v} \times \frac{\delta k}{2\ (D_v t)^{\frac{1}{2}}} \approx \frac{P}{2\ D_v (D_v t)^{\frac{1}{2}}}$$

$$> 10, \text{ and } \eta \beta^{-1/2} > 2 \tag{20}$$

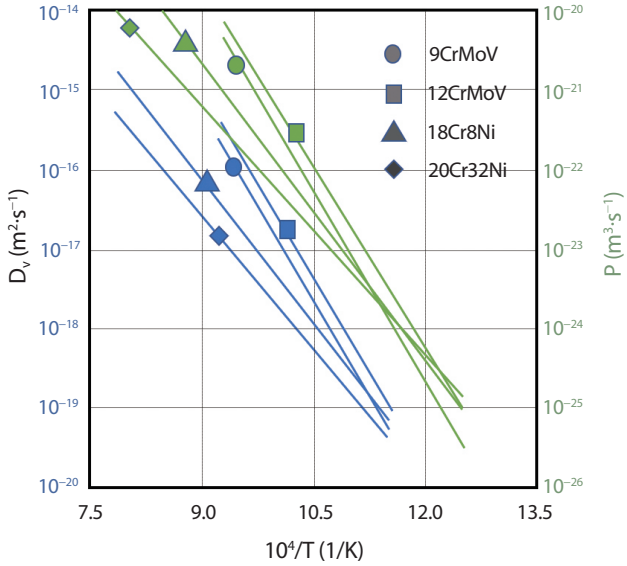

Fig. 2. Arrhenius plots for volume diffusion coefficients and triple product values P for grain boundary diffusion. Experimental diffusivity data of ferritic stainless steels 9CrMoV, 12CrMoV and austenitic stainless steels 18Cr8Ni and 20Cr32Ni were extracted from Z. Tökei et al. [24].

and the triple product of the grain boundary diffusivity as:

$$P \approx \beta \times 2\ D_v (D_v t)^{\frac{1}{2}} \tag{21}$$

For a precise determination of the triple product value P and ultimately, to find the solution for the GB diffusion equation [27], the conditions for both aforementioned equations must be met. In this context ^{51}Cr diffusion parameters of two ferritic-martensitic steels: 9CrMoV (P91), 12CrMoV, and the austenitic steels 18Cr8Ni (SS304) and 20Cr32Ni have been determined by Z. Tökei et al. [24] (Fig. 2).

As somewhat expected, ferritic/martensitic (FM) steel 9CrMoV (P91, or HT9) show higher volume and GB diffusion coefficients compared with austenitic steel at a given temperature and are therefore more prone to chromium depletion and matrix corrosion in contact with halide salt melts. FM steels, other than the austenitic steels, have a *bcc* crystal structure with lower atomic coordination number (CN 8 vs. CN 12) and less space filling (68% vs.

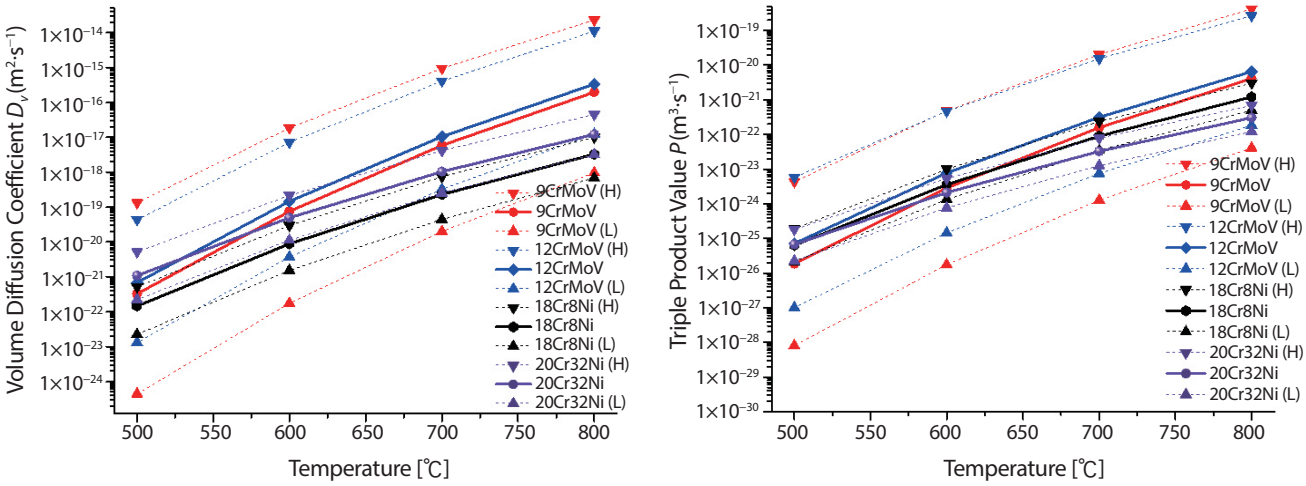

Fig. 3. Experimental uncertainties of determining Cr-self diffusivity: volume diffusion coefficients D_v and grain boundary triple product values P. Diffusion coefficients of ferritic-martensitic steels 9CrMoV, 12CrMoV show large standard deviations due to large variations of the activation energy. The notation (H) refers to the highest statistical limit, while (L) represents the lowest. Data were extracted from the equations published Z. Tökei et al. [24].

74%) compared with the austenitic *fcc* structures. In a first approximation, diffusivity is proportional to 1/CNτ where 1/τ is defined as the jump-rate frequency for vacancy diffusion. Hence, the higher atomic diffusivity measured for FM steels is explained by their lower atomic coordination numbers. Ferritic/martensitic steels also show higher activation energies for diffusion compared with austenitic steel. The activation energy Q for FM steels for volume diffusion was measured to 306 (± 29) kJ·mol^{-1} and 301 (± 15) kJ·mol^{-1} in the ferrite phase, versus 230 (± 7) kJ·mol^{-1} and 214 (± 6) kJ·mol^{-1} in the austenite phase of the austenitic 18Cr8Ni and 20Cr32Ni stainless, respectively [24]. The higher activation energies of FM steels imply stronger temperature dependency of diffusion rates compared with austenitic steels.

The Arrhenius plots (Fig. 2) do show noticeable data scattering and the statistical uncertainties and therefore standard deviations for the experimental determination of activation energies Q and the pre-exponential frequency factor D_0 are large. The experimental uncertainties of volume diffusion and GB diffusion for ferritic/martensitic and austenitic stainless steels for are shown in Fig. 3. At this, large standard deviation of the determined activation energy Q shows large impact when calculating volume diffusivity D_v and the triple product P for grain-boundary diffusivity. This is especially true for the FM steels 9CrMoV and 12CrMoV. Because Q defines the exponent, variations of Q, according to statistical uncertainties of 3 to 10%, can result in variations of volume diffusivity D_v and tripe product P (grain boundary diffusivity) over 1–4 orders in magnitude.

As a conclusion, the difference in chemical compatibility of ferritic/martensitic versus austenitic stainless steels with halite salt melts can be explained by considering volume self-diffusion coefficients of chromium. Diffusivity in Ferritic/martensitic stainless steel is noticeably larger than in austenitic stainless steels (Fig. 2). The knowledge of grain boundary diffusion coefficients and triple product values could, on the other hand, provide a true basis for corrosion modelling since microstructural information of the individual steel (heat, thermal treatment, cold-work) will be regarded. Steel is very much defined by its fabrication process and the subsequent heat treatment protocol to alter microstructural phases, grain sizes and defect concentration. Modelling efforts on steel properties must include these information which are somewhat convoluted in the yields when measuring grain boundary diffusion and triple point values for each steel at temperatures below 800°C. For

Table 2. Grain boundary diffusivity of ^{51}Cr tracer in SS-316 based steels [29, 30, 31]

Grain-boundary Diffusivity	Steel	Temperature range (°C)	Preexponential Factor ($m^3 \cdot s^{-1}$)	Activation Energy ($kJ \cdot mol^{-1}$)	Literature
^{51}Cr	Fe-17Cr-12Ni SS 316	576–1050	3.5×10^{-14}	151	Perkins et al. [26]
^{51}Cr	Fe-16.8Cr-11.4Ni-2.55 Mo – SS 316	650–1012	1.5×1^{-12}	191	Smith [27]
^{51}Cr	Fe-18Cr-12Ni -SS 316	700–950	1.2×10^{-10}	234	Cermak [28]
^{51}Cr	Fe-21Cr-31Ni	700–950	1.2×10^{-10}	234	Cermak [28]

high-temperature applications such as in MSR, structural steels of small grain sizes are widely preferred to optimize service life, even if these steels exhibit large specific grain boundary areas. The smaller the grain size, the greater the total grain boundary area available for boundary diffusion and the greater the importance of grain boundary diffusivity. Volume- or bulk diffusion coefficients reflect a single-crystal type situation and do not consider the nature of the individual microstructure. The interpretation of volume diffusion is most meaningful for materials of rather coarse grain structures and at high temperatures. For ferritic/martensitic or austenitic stainless steels volume diffusion is dominant at temperatures of 800°C or above and therefore beyond the range of MSR operation. Accurate knowledge on low temperature grain boundary diffusion of Cr in stainless steels or nickel-based alloys, on the other hand, could lay the foundation for meaningful computational estimations of the service life of structural steel and alloys under MSR conditions.

Literature data on ^{51}Cr grain boundary diffusion in austenitic steel do show large variations and experimental values for activation energy and pre-exponential frequency factor to differ (Table 2) also because alloy-specific heat- or solution treatment have massive impact on grain boundary diffusivity due to microstructural alterations.

As noted earlier, under the condition of mean diffusion distance $(D_v t)^{1/2}$ smaller than d/20 (d = average grain diameter), the grain boundary diffusivity can be extracted experimentally by ^{51}Cr tracer experiments as developed by Mizouchi et al. [26]. At this the triple product for grain boundary diffusivity is defined as:

$$P = D_b \delta k = 1.308\,(D_v t)^{1/2} - \left(\frac{\partial lnC}{\partial X^{\frac{6}{5}}}\right)^{-\frac{5}{3}} \qquad (22)$$

and the tail region in a logarithmic plot of tracer concentration C, or γ-activity of ^{51}Cr will vary linearly with penetration distance $X^{\frac{6}{5}}$ and the slope will yield the grain boundary diffusion coefficient D_b.

The grain boundary diffusivity is defined by the product of negative slope of $\left(\frac{\partial lnC}{\partial X^{\frac{6}{5}}}\right)^{-\frac{5}{3}}$ with 1.308 times the volume diffusion length and can vary by one to two orders in magnitude, depending on heat treatment [26]. With increasing heat treatment grain boundary diffusivity is decreased as a result of recrystallization and coarsening (grain growth). The magnitude of grain boundary diffusivity therefore depends greatly on the grain boundary characteristics [32] even if the diffusivity was calculated from the linear tail.

If the diffusion length is smaller than 1/20 of the grain boundary thickness δ, or $\delta > 20\,(D_v t)^{1/2}$, a type C diffusion kinetic instead of a type B kinetics is observed. Type C kinetic is observed for $X^{6/5} < 10\ \mu m^{6/5}$. For the product of segregation coefficient and grain boundary thickness (kδ) a value of 5 Å or 5×10^{-10} m is assumed.

Heat treatment (solution treatment, sensitizing) or mechanical deformation and defect accumulation (cold-work)

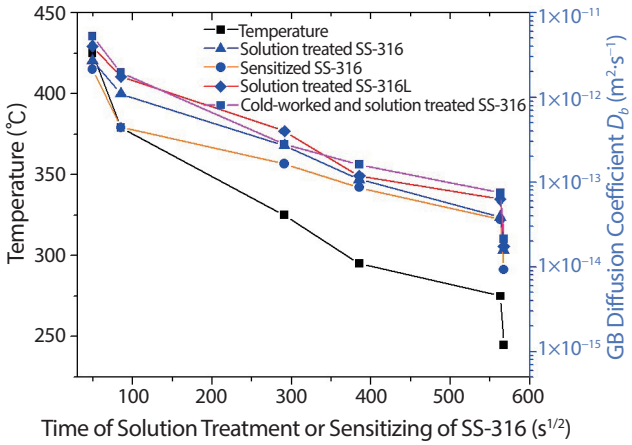

Fig. 4. Grain boundary diffusion coefficients of solution treated, sensitized, and cold-worked solution treated austenitic SS-316. Data were extracted from M. Mizouchi et al. [26].

of stainless steel will impact steel microstructure and therefore grain boundary diffusivity. In Fig. 4 grain boundary diffusivity of SS-316 after various thermal and mechanical treatments are sketched. At this, sensitized steel refers to steel with precipitation of carbides at the grain boundaries after heat treatment and solution treated steel to steel heat-treated in a way to dissolve this carbide precipitation. The cold-work is an attribute to an increase in defect concentration and microstructural changes by mechanical deformation (e.g. cold rolling). In Fig. 4 steels treated at rather low temperatures of 245–425°C are compared with steels after a heat treatment at higher temperatures of 720–900°C. For the low temperature data, the product of kδ (or sδ) was assumed to equal 0.5 nm (5 Å). In this respect, the triple product $P = k\delta D_b$ (or $s\delta D_{bg}$) of solution-treated, sensitized or cold-worked SS-316 at low temperatures (245–425°C) is noticeably lower than the values measured for solution-treated SS-316 (L) at 720–900°C. A triple product varies from between 10^{-24} $m^3 \cdot s^{-1}$ and 10^{-22} $m^3 \cdot s^{-1}$ at low temperature and between 10^{-20} $m^3 \cdot s^{-1}$ and 10^{-18} $m^3 \cdot s^{-1}$ at MSR-related temperatures. The activation energy for grain boundary diffusion of solution-treated, sensitized, or cold-worked and solution treated austenitic SS-316 stainless steels were all about 90 $kJ \cdot mol^{-1}$ [26]. Therefore, the temperature-dependency of grain-boundary diffusivity at low temperatures is rather moderate compared with the temperature dependency of diffusion of FM stainless steels investigated by Zökei et al. [24].

6. Experimental Corrosion Data on Structural Alloys for MSR Application

Chemical compatibility of structural alloys with halide salt melts is a lasting concern since the early days of liquid fuel nuclear reactors [1, 2, 3, 14] and further experimental work is a necessity in support of licensing. This is especially true for chloride based MSR systems featuring fast neutron spectra and utilizing ^{235}U, ^{239}Pu, and UNF for their fissile and fertile inventory. Even after 6+ decades of materials research, there is no obvious structural alloy for its deployment in fused chlorides in combination with hard neutron irradiation and large concentrations of fission products. Corrosion tests of structural alloys in halide salt melts are typically performed utilizing a dynamic approach mimicking reactor-type temperature and flow conditions. A great deal of excellent quality data from thermal- or forced convection loop-type corrosion tests were collected in the 1950s to the 1970s and chemical compatibility of mainly nickel-based alloys and austenitic stainless steels with fluoride melts were determined with the best possible approach and substantial experimental infrastructure. Static corrosion tests such as crucible tests or sealed capsule tests are far easier to conduct and can provide useful screening data. However, in crucible tests, samples and salt melt are protected by an inert cover gas and therefore vulnerable to increased oxygen and moisture contents in the salts. Open crucible tests are simple to conduct but are, as a result of their experimental simplicity, susceptible to increased impurity corrosion. On the other hand, impurity corrosion can be minimized while utilizing sealed crucible tests where capsules filled with salt are weld shut under inert conditions. However, as in loop testing, *in-situ* observations

Table 3. Corrosion data of Hastelloy N, Inconel alloys, Incoloy and stainless steel in hydrofluorinated LiF-BeF_2-ZrFe-UF_4 salt by loop testing in Hastelloy N container material. Data from [13, 22, 34, 35] were considered to estimate chromium depletion and to provide a projected overall chromium diffusion rate

Material	Temperature (°C)	Time (hours)	Mass Change ($mg \cdot cm^{-2}$)	Specific Mass Loss ($mg \cdot cm^{-2} \times day$)	Chromium-depletion rate ($\mu m \cdot year^{-1}$)	Chromium content (wt%)	Estimated total chromium diffusivity ($m^2 \cdot s^{-1}$)
Hastelloy N + Ti	676	1,610	−0.17	2.53×10^{-3}	28.60	7.3	1.21×10^{-15}
Hastelloy N	663	1,610	−0.4	5.93×10^{-3}	66.39	7.4	2.88×10^{-15}
Hastelloy N	685	17,719	−0.34	4.61×10^{-4}	5.13	7.4	2.23×10^{-16}
Hastelloy N + Ti	705	17,719	−0.52	7.04×10^{-4}	7.95	7.3	3.36×10^{-16}
Hastelloy N	705	17,719	−0.7	9.48×10^{-4}	10.56	7.4	4.58×10^{-16}
Hastelloy N	690	2,776	−0.15	1.30×10^{-3}	14.44	7.4	6.27×10^{-16}
Inconel Alloy 600	690	2,776	−0.49	4.24×10^{-3}	24.34	15	4.34×10^{-15}
Inconel Alloy 606	690	2,776	−6.6	5.71×10^{-2}	253.99	20	8.05×10^{-14}
Inconel Alloy 601	690	2,776	−16	1.38×10^{-1}	542.03	23	2.27×10^{-13}
Inconel Alloy 690	690	2,776	−55.5	4.80×10^{-1}	1,425.62	30	1.02×10^{-12}
Incoloy 811E	690	2,776	−117	1.01×10	4,450.96	21	1.56×10^{-12}
SS-304L	688	32,100	−63.6	4.76×10^{-2}	241.06	18	6.19×10^{-14}
Hastelloy N	704	4,984	−3.07	1.48×10^{-2}	164.60	7.4	7.15×10^{-15}
Inconel Alloy 601	704	1,828	−6.33	8.31×10^{-2}	325.65	23	1.37×10^{-13}
Hastelloy N	704	3,206	−0.94	7.04×10^{-3}	78.35	7.4	3.40×10^{-15}
Hastelloy N	704	10,000	−3.35	8.04×10^{-3}	89.52	7.4	3.89×10^{-15}
Hastelloy N	704	4,309	−2.31	1.29×10^{-2}	143.25	7.4	6.22×10^{-15}

are not feasible. An excellent summary and analysis of 60+ corrosion studies published between 1960 and 2016 using fluoride and chloride salt melt was recently provided by Raiman & Lee (2018) [33]. The results on mass changes or specific mass losses do vary with methodology and experimental set-up of each data but overarching quantitative statements can hardly be made besides some generalities. In order to potentially link kinetic information on chromium diffusivity to actual corrosion rates, data from long-term loop testing might serve best for this purpose since impurity corrosion is most likely excluded. Using purified, oxygen- and moisture free salt is therefore of high relevance. As expected, loop-testing was mainly performed with Hastelloy N (alias Alloy N or INOR-8) in fluoride salt melts at 663 to 705°C. In this respect, the results of the most impressive 1,610 to 32,100 hours (≈ 3.7 years) loop testing by Koger [13, 22] and Keiser [34, 35] are best suited for the following interpretation of chromium based MSR containment corrosion (Table 3). The results of these state-of-the-art experiments will be used to eventually extract an estimate mixed volume- and grain boundary diffusivity of chromium in Ni-based alloys and stainless steel. During salt loop experiments chromium concentration do increase and additional increase of molybdenum- and niobium concentration were

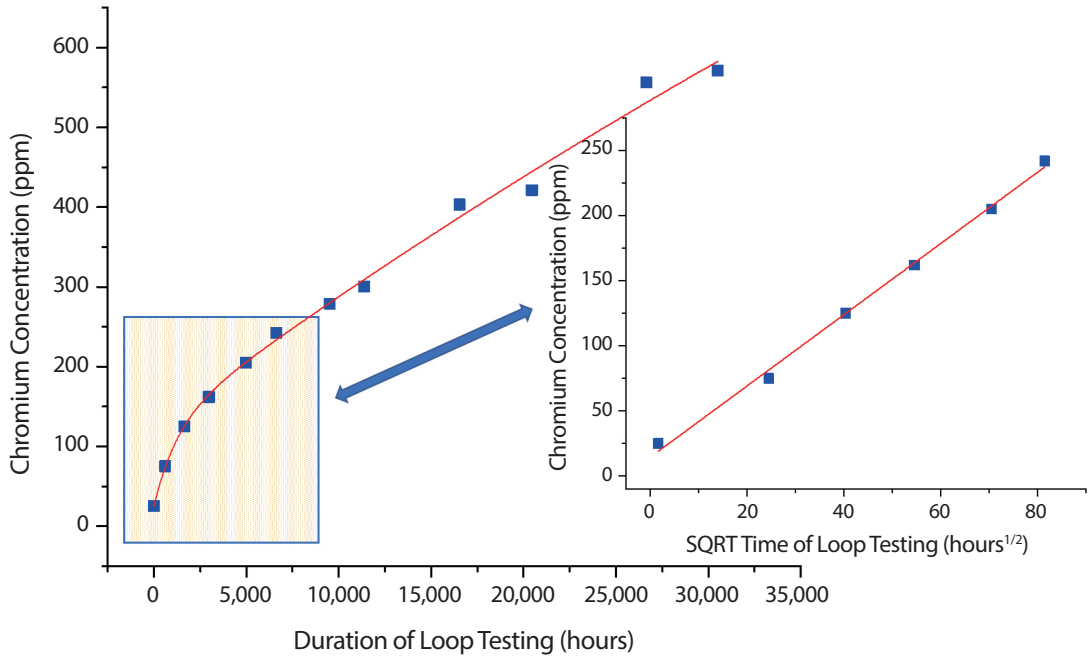

Fig. 5. Chromium concentration in fluoride salt Hastelloy N test loop with time. Cr concentration increase with 1st order kinetics for about 10,000 hours followed by a linear increase of about 0.48 pm per day. Data were extracted from Koger [22].

measured in the fluoride salt as well [22]. However, after a nine-year experiment chromium concentration in the fluoride salt reaching 1,700 ppm, the concentrations of Mo and Nb were only 23 ppm and 87 ppm, respectively.

Salt analysis shows that it is safe to assume that the mass-loss of containment alloys in fluorite salt melts is mainly related to the depletion of chromium at the alloy-salt interface. We can therefore define the alloy corrosion rates as a chromium-depletion rates where the chromium content lowers continuously from the nominal content in the bulk, 7.4wt% for Hastelloy N, towards the alloy salt interface. For reasons of simplification, in Table 3 (right column) the Cr-content at the interface is set to 0wt% with a linear gradient towards the bulk. Based on this assumption, the chromium deletion rates are calculated to about 5–160 μm·year^{-1} for Hastelloy N, 24-1, 425 μm·year^{-1}, 240 μm·year^{-1} for SS-304L, and as much as 4,451 μm·year^{-1} for Incoloy. With high chromium content in structural alloys (Inconel, Incoloy) chromium depletion is more pronounced. Overall, Hastelloy N performs exceptionally well in fluoride salts and the large variations in the experimental results (5–160 μm·year^{-1}) is related to the individual experimental set-up. Based on estimated chromium depletion, the total chromium diffusivity, including both: volume diffusion and grain boundary diffusion can be extracted as estimates (Table 3). The projected Cr-diffusivities are a combination of bulk and grain boundary diffusion and are therefore larger than Cr volume diffusion coefficients of ferritic and austenitic steels (2×10^{-19} to 6×10^{-18} m^2·s^{-1}, Fig. 2), but smaller than grain boundary diffusion coefficients for chromium in austenitic SS-316 (9×10^{-15} to 5×10^{-12} m^2·s^{-1}, Fig. 4). This fact provides credibility to the technical approach obtaining these estimates. Unfortunately, it is not possible to purely extract grain boundary diffusivity and the triple product *P* from these legacy data. However, these estimates can be used to trace the kinetics of alloy corrosion in fluoride salt melts but less so for chloride salt melts where besides Cr, also Mo, Fe, and Ni will form metal chlorides. The

Table 4. Evaluation of the specific mass loss of Hastelloy N based on measured chromium concentration in fluoride salt melt [22]

Pipe Material: 3/8-inch Alloy N with 7.4wt% Cr	Salt: 70mol% LiF-23mol% BeF_2–ZrF_4 5mol% -UF_4 1mol%-ThF_4 1mol%
Volume for a 10 mm segment: 712.6 mm^3 ≈ 0.7 mL	Molarity: 134 $mol \cdot mL^{-1}$ or 0.134 $mol \cdot mL^{-1}$
Area of a 10 mm segment: 299 mm^2 ≈ 3 cm^2	Test period: 30,000 hours = 1,250 days
Mass Loss: 0.268 mg $Cr \cdot cm^{-2} \cdot 30{,}000\ hours^{-1}$	Cr-content: 600 ppm = 0.08 $mol \cdot L^{-1}$ Cr-content ≈ 0.575 $g \cdot L^{-1}$
Estimated Specific Mass Loss: 2.147×10^{-4} $mg \cdot cm^{-2} \cdot day^{-1}$	Cr-content per mL: 0.575 mg
Average Specific Mass Loss measured by [19]: 1.98×10^{-3} $mg \cdot cm^{-2} \cdot day^{-1}$	Cr-content per cm^2: 0.134 mg
Projected Mass Loss after 9.2 years testing and a final Cr concentration of 1,700 ppm [19]: 2.50×10^{-4} $mg \cdot cm^{-2} \cdot day^{-1}$	Cr-content considering a surge tank volume equal to pipe volume: 0.268 mg $Cr \cdot cm^{-2}$

corrosion and degradation of structural alloys in chloride salt melts is therefore more pronounced. On the other hand, the formation of a variety of metal chlorides offers alternative ways for enhanced corrosion monitoring of structural alloys in future MSR designs.

7. Corrosion Monitoring in Future MSR Designs

Long-term corrosion loop testing using Hastelloy N have shown that chromium concentration in fluoride salt melts increases with 1st order kinetics and therefore linear with time^{½} within the first ≈10,000 hours (13–14 months). With ongoing corrosion, chromium concentration increases approximately linear with time, besides some scattering. The overall trend of chromium concentration in the halide salt can be modelled with an exponential decay function and reflects the specific mass loss of Hastelloy N mainly based on its Cr depletion at the alloy salt interface. Following the period of 1st order kinetics, chromium concentration in the fluoride salt loop increases fairly linear with time, allowing for simple long-term projections for the specific mass loss of the structural containment alloy (Fig. 5).

The progression of chromium concentration during the long-term salt loop experiment by Koger [22] can be used to also evaluate specific mass loss of other containment alloys since the corrosion characteristics might be very similar. The simplicity and predictability of chromium concentration increase during corrosion provides a strong argument for online monitoring since deviations from 1st order kinetics or linearity are easily observed. The discribed increase in chromium concentration in the salt melt during MSR operation is linked to the specific mass loss of the containment alloy subjected to homogeneous matrix corrosion. Deviations from this projected trend would indicate e.g. pitting corrosion or grain boundary embrittlement.

In the following, an attempt is made to derive mass-loss data through the progression of chromium concentration during loop testing. In the loop testing by Koger [22] Hastelloy N tubing with a 3/8-inch inner diameter was used and, assuming the salt volume in the surge tank is about the same than the overall inner tube volume the specific mass loss of Hastelloy N can be discussed (Table 4). At this, a pipe segment with a unit length of 10 mm is considered, with a volume of 0.7 mL and an inner surface are of 3 cm^2. The salt (70mol% LiF-23mol% Be–ZrF_4 5mol%-UF_4 1mol%–ThF_4 1mol%) has a molar mass of 19.8 $g \cdot mol^{-1}$, a calculated density of 2.654 $g \cdot cm^{-3}$ and an estimated molarity of 134 $mol \cdot L^{-1}$. As shown in Fig. 5, the chromium

concentration increased by 600 ppm within 30,000 hours (linear projection) or 0.48 ppm chromium per day.

Using these chromium concentration data from loop testing, a computational specific mass loss of 2.15×10^{-4} $mg \cdot cm^{-2} \cdot day^{-1}$ and 2.5×10^{-4} $mg \cdot cm^{-2} \cdot day^{-1}$ is estimated for 4.8 years and 9.2 years corrosion testing, respectively. The real measured specific mass loss, however, was 1.98×10^{-3} $mg \cdot cm^{-2} \cdot day^{-1}$ in average. This significant discrepancy can partly be explained by the nature of loop testing, where material gets dissolved at the hot leg and material deposits at the cold leg. However, monitoring of chromium concentration in halide salt melts can provide crucial information on corrosion to project the specific mass loss of structural alloys, even if the computational specific mass loss might understate actual containment corrosion by one order in magnitude, as demonstrated in Table 4. In long-term loop testing the chromium concentration of Hastelloy N at the salt interface is reduced from 7.4wt% to 0.5wt% and further the iron content from 4.5wt% to < 0.5wt% [22]. The consideration of additional metal halide concentration can therefore be helpful to provide a more accurate projection on containment corrosion. In this respect, the use of chloride salts as coolant and/or fuel is beneficial since metals like Cr, Fe, Mo, Ni become soluble as chlorides and monitoring the progress of their concentration during MSR operation will provide an essential tool for tracing alloy corrosion and therefore optimizing containment service life. Under MSR conditions metal chloride concentration should also follow, after an incubation period with 1st order kinetics, a linear projection with a positive slope and a steady increase of sub-ppm level per day. The progression of the individual metal chloride concentration should reflect the alloy composition and the wt% ratio of the alloying constituency in consideration of their diffusivity. This ideal scenario would reflect homogeneous matrix corrosion at the alloy – salt interface including near-surface void formation. A sharp increase in the metal chloride concentration could, on the other hand, provide warning for potential material failure eventually caused by severe intergranular cracking or pitting corrosion, far ahead in time and before this problem can cause an issue. Continuous monitoring of alloying metal chloride concentrations can therefore aid in optimizing containment service life and provides direct information about the nature of the ongoing corrosion scenario and can set indicators for timely warnings of potential material failure in the near future.

8. Irradiation-induced Alteration of Corrosion Properties

While irradiation induced changes in tensile- and mechanical properties will be reversed by defect annihilation and recrystallization at high operational temperatures, the formation of irradiation-induced precipitates, on the other hand, could very well alter corrosion properties of the selected containment alloy because of the depletion of alloying metal concentrations in the vicinity of the precipitates and the formation of decomposition phases in the steel matrix. The formation of radiation-induced precipitates (RIP) do not directly initiate the failure of structural components, but it can strongly alter their corrosion behavior [36, 37]. Radiation-induced segregation (RIS) will result in chromium depletion at grain boundaries which not only alters corrosion resistance of grain boundaries, but also enhances irradiation assisted stress corrosion cracking in stainless steel. This is a concern for structural alloys exposed to high neutron fluencies and can endanger their physico-mechanical integrity. The local constitutional variation caused by RIS can lead to a decomposition of the austenitic fcc γ-phase to form γ' or, in FM steels, the ferritic α phase to form additional Cr-rich bcc α'. In addition to these matrix effects by RIS in austenitic steel, metal carbides (MC) and Fe_2P precipitate as a result of Ni- and Si segregation and a last stage η-carbides M_6C ($M_{23}C_6$) and G-phase silicide form, also indicating the onset of loss of radiation stability.

In austenitic steel, radiation-induced precipitation will lower the concentration of alloying constituency in the

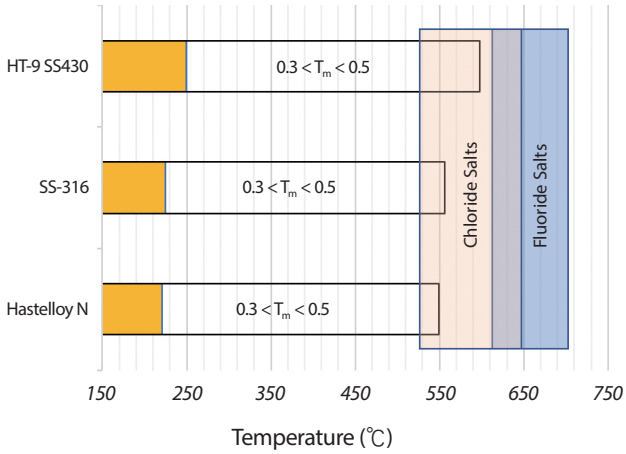

Fig. 6. Susceptibility of structural alloys for suffering from radiation damage effects in the temperature regime of chloride- and fluoride-based MSR designs.

steel matrix and will noticeably reduce the content in Mn, Si, P, Cr and Ni, and therefore increase its susceptibility for corrosion. The evolution of this defect microstructure in austenitic steel during irradiation is a constant competition between the phases to mitigate void swelling (MC, Fe_2P) and the phases formed through the partly decomposition of γ (γ', G-phase, η-carbides) [37, 38]. This competing effect among precipitates is impacted by thermal or thermo-mechanical treatment.

In ferritic-martensitic steel, irradiation induced precipitates like η-carbides, χ-phases, α' and σ-phases contain high concentrations in Cr, Mo, Si, W, and V, therefore depleting the content of alloying metals in the ferritic steel matrix and reducing the resistance to corrosion. The bcc α' phase, e.g., contains predominantly chromium and precipitates uniformly as nano-sized particles within the ferrite and the tempered martensite phase. This demixing of chromium in the ferritic-martensitic steel matrix as a radiation-damage indicator will enhance its vulnerability to the redox-based corrosive attack expected in MSR operations.

The rather high and constant temperatures of slightly > 0.5 T_m during the operation of fluoride salt based MSR designs will vastly mitigate irradiation induced alterations of tensile- and mechanical properties as well as segregation and precipitations (RIS, RIP) within the alloy microstructure. Therefore, large alterations to the corrosion resistance of structural containment alloys during the operations of fluoride salt based MSR designs are not expected. Irradiation-induced void swelling is mitigated by increasing temperature but enhanced by the lack of RIP, and therefore some degree of void swelling must be considered. In Fig. 6 the temperature range $0.3 < T_m < 0.5$ for Hastelloy N, austenitic stainless-steel and ferritic-martensitic steel are sketched for operational temperature range of fluoride- and chloride based MSR concepts. In the temperature window of fluoride based MSR designs structural alloys are not susceptible to suffer from radiation damage effects. On the other hand, in the lower temperature window of chloride based MSR concepts, structural alloys such as Hastelloy N, austenitic stainless steel and ferritic/martensitic steel radiation damage effects and therefore increased containment corrosion must be considered.

9. Conclusion

This paper is an evaluation of experimental literature MSR data in order to project qualitative and semi-quantitative information on containment corrosion expected in chloride-based MSR designs and its relevance to the prospect of online monitoring of alloying metal halides concentrations during MSR operation in future designs. Continuous monitoring of alloying metal chloride concentrations can aid in optimizing containment service life and provides direct information about the nature of the ongoing corrosion scenario and can set indicators for timely warnings of potential material failure in the near future. A sharp increase in the metal chloride concentration could provide warning for potential material failure eventually caused by severe intergranular cracking or pitting corrosion, far ahead in time and before this problem can cause an issue.

MSR containment corrosion in chloride salt systems is more pronounced and complex than in fluoride salt systems

and at the alloy salt interface, stable alloying metal chloride species of Cr, Mn, Fe, Co, Ni, and Mo will form. The build-up and the progression of the metal chloride species concentration depend on the redox condition of the fuel e.g. U^{4+}/U^{3+}, specification and microstructure of the deployed containment alloy, salt temperature, time, and the additional build-up of fission products. The metal chloride concentrations during MSR operation will probably increase with 1st order kinetics and linearly with time$^{1/2}$ for an incubation period of about 10,000 hours (13–14 months). Thereafter, metal chloride concentrations will probably follow a linear projection with a positive slope and a steady increase of ppm level per day if homogeneous matrix corrosion is preserved.

While the thermodynamic basis of chromium depletion in structural alloys is based on redox-reactions and free Gibbs energies and therefore rather straightforward, our knowledge about the underlying kinetics of containment alloy corrosion is not as settled. However, it is agreed that the yield of chromium self-diffusion in structural alloys does propel the kinetics of stainless-steel corrosion in molten halides. Diffusivity in structural alloys under MSR operation temperatures (550°C to 700°C) is mainly defined as diffusion along selected paths and therefore grain boundary diffusion is dominant over volume diffusivity. The knowledge of grain boundary diffusion coefficients and the associate triple product values of the specific containment alloy could provide a true basis for future corrosion modelling since important microstructural information of the individual steel (heat, thermal treatment, cold-work) will be included as essential factors.

Online monitoring of metal chloride concentration such as $CrCl_2$, $CrCl_3$ during MSR operation can provide direct information about the mechanism of ongoing containment corrosion. The progression of chromium concentration can be used to evaluate the specific mass loss of the containment alloy since their characteristics in yields over time are similar. However, the computational specific mass loss of structural alloys based on metal chloride concentrations in the salt, strongly understates actual containment corrosion, which must be further investigated.

In austenitic steel, radiation-induced precipitation will lower the concentration of alloying constituency in the steel matrix and will noticeably reduce the content in Mn, Si, P, Cr and Ni, and therefore increase its susceptibility for corrosion. In ferritic-martensitic steel, irradiation induced precipitates like η-carbides, χ-phases, α' and σ-phases contain high concentrations in Cr, Mo, Si, W, and V, therefore depleting the content of alloying metals in the ferritic steel matrix and reducing the resistance to corrosion. Therefore, the demixing of chromium in austenitic or ferritic-martensitic stainless-steel matrixes will enhance its vulnerability to the corrosive attack in MSR operations towards higher radiation dose and with longer service life. Chloride-based MSR concepts operate at lower temperature compared with fluoride-based designs, making structural alloys more susceptible for radiation damage effects and are therefore more prone to corrosive attack.

Acknowlegements

Pacific Northwest National Laboratory is operated by Battelle Memorial Institute for the U.S. Department of Energy under Contract No. DE-AC05-76RL01830.
This work was supported by the U.S. Department of Energy, Office of Nuclear Energy.

REFERENCES

[1] E.S. Bettis, R.W. Schroeder, G.A. Cristy, H.W. Savage, R.G. Affel, and L.F. Hemphill, "The Aircraft Reactor Experiment-Design and Construction", Nucl. Sci. Eng., 2, 804-825 (1957).
[2] W.D. Manly, G.W. Adams, J.H. Coobs, J.H. DeVan, D.A. Douglas, E.E. Hoffman, and P. Patriarca. Aircraft Reactor Experiment – Metallurgical Aspects, Oak Ridge

National Laboratory Report, 29, ORNL-2349 (1957).

[3] W.D. Manly, J.H. Coobs, and J.H. DeVan, "Metallurgical Problems in Molten Fluoride Systems", Prog. Nucl. Energy, 2, 4 (1960).

[4] J.H. DeVan and R.B. Evans. Corrosion Behavior of Reactor Materials in Fluoride Salt Mixtures, Oak Ridge National Laboratory Technical Report, ORNL/TM-328 (1962).

[5] V. Ignatiev and A. Surenkov, "5.10-Material Performance in Molten Salts", in: Comprehensive Nuclear Materials, R.J.M. Konings, eds., 221-250, Elsevier, Amsterdam (2012).

[6] J.R. DiStefano, J.H. DeVan, J.R. Keiser, R.L. Klueh, and W.P. Eathery, "Materials Consideration for Molten Salt Accelerator-based Plutonium Conversion Systems", Oak Ridge National Laboratory Report, Oak Ridge National Laboratory, ORLN/TM-12925 (1995).

[7] Elysium Industries. "The Molten Chloride Salt Fast Reactor." Elysium Industries. Accessed Apr. 08 2021. Available from: http://www.elysiumindustries.com/technology.

[8] TerraPower LLC. "TerraPower's Molten Chloride Fast Reactor Technology: Retooling Nuclear for a Changing Energy Sector." TerraPower LLC. Accessed Apr. 08 2021. Available from: https://www.terrapower.com/wp-content/uploads/2020/08/TP_2020_MCFR_Technology_082020.pdf.

[9] Moltex Energy. "Moltex's Stable Salt Reactor – Wasteburner (SSR-W) Uses the Nuclear Waste From Past and Present Operations as Fuel, Significantly Reducing Waste Stockpiles." Moltex Energy. Accessed Apr. 08 2021. Available from: https://www.moltexenergy.com/reduces-waste/.

[10] D.E. Holcomb, G.F. Flanagan, B.W. Patton, J.C. Gehin, R.L. Howard, and T.J. Harrison. Fast Spectrum Molten Salt Reactor Options, Oak Ridge National Laboratory Report, ORNL/TM-2011/105 (2011).

[11] O. Beneš and R.J.M. Konings, "Thermodynamic Evaluation of NaCl-$MgCl_2$-UCl_3-$PuCl_3$ System", J. Nucl. Mater., 375(2), 202-208 (2008).

[12] R.E. Thoma. Phase Diagrams of Nuclear Reactor Materials, Oak Ridge National Laboratory Technical Report, ORNL 2548 (1959).

[13] J.W. Koger. Alloy Compatibility With LiF-BeF_2 Salts Containing ThF_4 and UF_4, Oak Ridge National Laboratory Report, ORNL/TM-4286 (1972).

[14] J.A. Lane, H.G. MacPherson, and F. Maslan, Fluid Fuel Reactors, Addison-Wesley Publishing Company Inc., Massachusetts (1958).

[15] J. Busby, L.M. Garrison, L. Lin, S.S. Raiman, S. Sham, C. Silva, H. Wang, R. Iyengar, and G. Tartal. Technical Gap Assessment for Materials in Component Integrity Issues for Molten Salt Reactors, Oak Ridge National Laboratory Technical Report, ORNL/SPR-2019/1089 (2019).

[16] Australian Stainless Steel Development Association. "304: The Place to Start." ASSDA. Accessed Apr. 08 2021. Available from: https://www.assda.asn.au/technical-info/grade-selection/304-the-place-to-start.

[17] Australian Stainless Steel Development Association. "316: The First Step up." ASSDA. Accessed Jul. 30 2020. Available from: https://www.assda.asn.au/technical-info/grade-selection/316-the-first-step-up.

[18] J.R. Keiser, J.H. Devan, and E.J. Lawrence, "Compatibility of Molten Salts With Type 316 Stainless Steel and Lithium", J. Nucl. Mater., 85-86, 295-298 (1979).

[19] C.F. Baes, "The Chemistry and Thermodynamics of Molten Salt Reactor Fuels", J. Nucl. Mater., 51(1), 149-162 (1974).

[20] J.A. Plambeck, "Electromotive Force Series in Molten Salts", J. Chem. Eng. Data, 12(1), 77-82 (1967).

[21] S. Guo, J. Zhang, W. Wu, and W. Zhou, "Corrosion in the Molten Fluoride and Chloride Salts and Materials Development for Nuclear Applications", Prog. Mater. Sci., 97, 448-487 (2018).

[22] J.W. Koger. Evaluation of Hastelloy N Alloys After Nine Years Exposure to Both a Molten Fluoride Salt and air at Temperatures From 700 to 560°C, Oak Ridge

National Laboratory Report, ORNL/TM-4189 (1972).

[23] R.B. Evans, J.H. DeVan, and G.M. Watson. Self-diffusion in Nickel-base Alloys, Oak Ridge National Laboratory Report, ORNL-2982 (1961).

[24] Z. Tökei, K. Hennesen, H. Viefhaus, and H.J. Grabke, "Diffusion of Chromium in Ferritic and Austenitic 9–20wt% Chromium Steels", Mater. Sci. Technol., 16(10), 1129-1138 (2000).

[25] L.G. Harrison, "Influence of Dislocations on Diffusion Kinetics in Solid With Particular Reference to the Alkali Halides", Trans. Faraday Soc., 57, 1191-1199 (1961).

[26] M. Mizouchi, Y. Yamazaki, Y. Iijima, and K. Arioka, "Low Temperature Grain Boundary Diffusion of Chromium in SUS316 and 316L Stainless Steel", Mater. Trans., 45(10), 2945-2950 (2004).

[27] T. Suzuoka, "Lattice and Grain Boundary Diffusion in Polycrystals", Trans. Jpn. Inst. Met., 2(1), 25-32 (1961).

[28] G.B. Gibbs, "Grain Boundary Impurity Diffusion", Phys. Status Solidi B, 16(1), K27-K29 (1966).

[29] R.A. Perkins, R.A. Padgett, and N.K. Tunali, "Tracer Diffusion of ^{59}Fe and ^{51}Cr in Fe-17 wt Pct Cr-12 wt Pct Ni Austenitic Alloy", Metall. Mater. Trans. B, 4, 2535-2540 (1973).

[30] A.F. Smith, "The Diffusion of Chromium in Type 316 Stainless Steel", Met. Sci., 9(1), 375-378 (1975).

[31] J. Cermak, "Grain Boundary Self-diffusion of ^{51}Cr in Fe-Cr-Ni Alloys", Z. Metallkd., 81(3), 193-195 (1990).

[32] A.P. Sutton and R.W. Balluffi, Interfaces in Crystalline Materials, Clarendon Press, Oxford (1995).

[33] S.S. Raimanm and S. Lee, "Aggregation and Data Analysis of Corrosion Studies in Molten Chloride and Fluoride Salts", J. Nucl. Mater., 511, 523-535 (2018).

[34] J.R. Keiser, D.L. Manning, and R.E. Clausing, "Corrosion Resistance of Some Nickel-Based Alloys in Molten Fluoride Salts Containing UF_4 and Tellurium", Proc. of the 1st Int. Symp. On Molten Salts, vol.1976-6, 315-328, The Electrochemical Society, New York (1976).

[35] J.R. Keiser. Compatibility Studies of Potential Molten-Salt Breeder Reactor Materials in Molten Fluoride Salts, Oak Ridge National Laboratory Report, ORNL/TM-5783 (1977).

[36] G.S. Was, J. Busby, and P.L. Andresen, "Effect of Irradiation on Stress-Corrosion Cracking and Corrosion in Light Water Reactors", in: Corrosion: Environments and Industries, S.D. Cramer and B.S. Covino, eds., vol. 13C, 386-414, ASM International, Ohio (2006).

[37] T.R. Allen and J.T. Busby, "Radiation Damage Concerns for Extended Light Water Reactor Service", JOM, 61(7), 29-34 (2009).

[38] F.A. Garner, "Irradiation Performance of Cladding and Structural Steels in Liquid Metal Reactors", in: Materials Science and Technology – A Comprehensive Treatment, R.W. Cahn, P. Haasen, and E.J. Kramer, eds., 419-543, VCH Publishers Inc., New York (1994).